

On the Complex Structural Picture of the Ionic Conductor $\text{Sr}_6\text{Ta}_2\text{O}_{11}$

Niina Jalarvo,^{*,†,‡} Simone Casolo,[§] Nadir Aliouane,^{||,⊥} Dirk Wallacher,[¶] Ole Martin Løvvik,^{#,□} and Truls Norby^{*,†}

[†]Department of Chemistry, University of Oslo, SMN/FERMiO, Gaustadalleen 21, NO-0349 Oslo, Norway

[‡]Jülich Centre for Neutron Science JCNS-1, Forschungszentrum Jülich GmbH, Outstation at Spallation Neutron Source at Oak Ridge National Laboratory, Chemical and Engineering Materials Division, P.O. Box 2008, 1 Bethel Valley Road, Oak Ridge, Tennessee 37831-6475, United States

[§]Dipartimento di Chimica, Università degli Studi di Milano, via Golgi 19, 20133 Milan, Italy

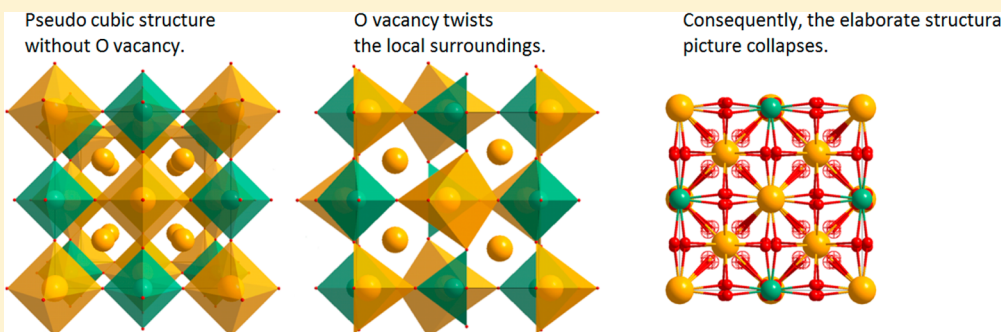
^{||}Physics Department, Institute for Energy Technology, P.O Box 40, NO-2027 Kjeller, Norway

[⊥]Laboratory for Neutron scattering, Paul Scherrer Institute, CH5232 Villigen PSI, Switzerland

[¶]Helmholtz-Zentrum für Materialien und Energie GmbH, Hahn-Meitner Platz 1, D-14109 Berlin, Germany

[#]SINTEF Materials and Chemistry, NO-0314 Oslo, Norway

[□]Department of Physics, University of Oslo, NO-0315 Oslo, Norway



ABSTRACT: $\text{Sr}_6\text{Ta}_2\text{O}_{11}$ presents an interesting model system of a highly defective and disordered complex perovskite, exhibiting oxide ion conductivity at high temperatures as well as proton conductivity when hydrated by presence of water vapor. In this paper, we present a comprehensive structural study of $\text{Sr}_6\text{Ta}_2\text{O}_{11}$ in its dry and hydrated state, based on DFT calculations and NPD measurements. At low temperatures, dry $\text{Sr}_6\text{Ta}_2\text{O}_{11}$ has a tetragonal symmetry with ordered oxygen vacancies. The oxygen vacancy induces perturbations to its near surroundings, disturbing particularly the A site cations. As a consequence, the elaborate structural picture collapses at higher temperatures. The high-temperature structure has a cubic symmetry with fractionally occupied structural oxygen sites and disorder on the oxygen and strontium sublattices. The structure of the fully hydrated compound $\text{Sr}_6\text{Ta}_2\text{O}_{10}(\text{OH})_2$ was determined as monoclinic with significant distortions of the anion and metal cation sites.

INTRODUCTION

Oxygen deficient perovskites are of interest as potential electrolytes for solid oxide fuel cells (SOFCs)^{1–4} exhibiting oxide ion (vacancy) conduction in dry atmospheres and in some cases proton conduction in wet atmospheres.^{5–7} Structural features such as the distribution of oxygen vacancies affect hydration thermodynamics and the mobility of defects. Furthermore, a key question for proton conduction is their distribution in the hydrated analogues. Such aspects are often problematic to study by structural analysis tools since the concentrations of oxygen vacancies and protons are in many cases low and because most of the conventional techniques probing crystal structures are not adequate to detect light elements, for example, hydrogen or oxygen.

In this work, we report results of neutron powder diffraction (NPD) combined with density functional theory (DFT) first principle calculations of $\text{Sr}_6\text{Ta}_2\text{O}_{11}$, which may also be written $\text{Sr}_4(\text{Sr}_2\text{Ta}_2)\text{O}_{11}$ or $\text{Sr}_4(\text{Sr}_2\text{Ta}_2)\text{O}_{11}\text{v}_\text{O}$ (where v_O denotes oxygen vacancy), that is, an oxygen deficient complex perovskite hosting one vacant out of 12 oxide ion sites. In humid atmospheres, this perovskite will hydrate into $\text{Sr}_6\text{Ta}_2\text{O}_{11}\times\text{H}_2\text{O}$,^{8,9} which more correctly may be taken to be an oxohydroxide, $\text{Sr}_6\text{Ta}_2\text{O}_{10}(\text{OH})_2$. This material has considerable ionic conductivities¹⁰ and the relatively high concentration of oxygen vacancies and protons makes it possible to

Received: November 15, 2012

Revised: April 12, 2013

Published: April 15, 2013

experimentally study their distributions in the crystal structure, hence making the material an interesting model system for highly defective and disordered complex perovskite. Traditionally ion conduction in solids is described as thermally activated jumps. However, recent studies on oxygen deficient perovskites, for example, SrFeO_{3-x} ^{11–13} SrCoO_{3-x} ^{11,14,15} and CaFeO_{3-x} ¹¹ ($0 \leq x \leq 0.5$), realize that ion conduction concept comprise diverse features like oxygen diffusion via lattice instabilities and internal dynamically triggered interphases. Better understanding of the defect distribution and the disorder in $\text{Sr}_6\text{Ta}_2\text{O}_{11}$ can help to understand related systems as well, where similar features concerning the origin and distribution of defects exist.

Animitsa et al.¹⁶ studied the crystal structure of $\text{Sr}_6\text{Ta}_2\text{O}_{11}$ and $\text{Sr}_6\text{Ta}_2\text{O}_{10}(\text{OH})_2$ by X-ray powder diffraction (XRPD) at room temperature. Their work showed that the dry material has a cubic cryolite structure (perovskite related structure with B sites occupied with two different types of atoms in a 1:1 ratio and NaCl type ordering) with space group $Fm\bar{3}m$, and lattice parameter $a = 8.32 \text{ \AA}$. A water uptake of 0.5 mol/molecular unit (half of the theoretical value) did not change the crystal structure, but beyond that value a structural change was induced to an orthorhombic space group $Fmmm$ with only a small difference of the unit cell parameters compared to the dry cubic phase. The oxygen coordinates were determined with large uncertainties, and information about the oxygen vacancy distribution was not obtained. A Raman spectroscopy study of $\text{Sr}_6\text{Ta}_2\text{O}_{11}$ at room temperature showed signs of short-range disorder on the oxygen and cation lattices.¹⁷ Furthermore, Ashok studied the structure by transmission electron microscopy (TEM)¹⁸ and found in her samples domains containing different crystal structures: cubic, hexagonal, and tetragonal. The most relevant structure observed for the dry sample belongs to the hexagonal space group $P\bar{6}2m$, and it shows ordered oxygen vacancies, which approximately tripled the c -axis compared to the previously reported cubic model. The structure of the hydrated sample was determined as tetragonal with space group $I4_1$. All the structural studies cited above were conducted at room temperature, but the TEM studies were additionally carried out in high vacuum, and it is likely that the hydrated sample may have lost water under the electron beam.

None of the above-mentioned techniques could give a comprehensive picture of the defect distribution in $\text{Sr}_6\text{Ta}_2\text{O}_{11}$ and thus the understanding of the disordered character remains rather vague. In this work, we have studied strontium tantalate over a large temperature range with NPD, which is capable to detect light elements like oxygen and hydrogen, in combination with XRPD and DFT calculations, in order to draw a more complete picture about the $\text{Sr}_6\text{Ta}_2\text{O}_{11}$ structure in its dry and hydrated forms.

EXPERIMENTAL AND COMPUTATIONAL METHODS

Sample Preparation. The $\text{Sr}_6\text{Ta}_2\text{O}_{11}$ samples were prepared by a solid state method. Commercially available high purity powders Ta_2O_5 (99.9% from Sigma Aldrich) and SrCO_3 (99.9% from Sigma Aldrich) were first calcined to remove water, weighed in appropriate amounts, mixed, and annealed in ambient air as follows: 800 °C, 10 h; 950 °C, 10 h; 1100 °C, 10 h; and finally sintered at 1500 °C for 30 h in dry Ar atmosphere to avoid any carbonization, hydroxylation, hydration, or water insertion. Prior to each heat treatment, the samples were pressed into pellets. Between each stage the

pellets were reground in an agate mortar, followed by 1 h ball milling in isopropanol, which was then evaporated at 150 °C before the powder was pressed into pellets again. After sintering the samples were kept in a dry Ar atmosphere, for transportation the samples were placed in a small desiccator with P_2O_5 and KOH as desiccants and CO_2 trap. Before the diffraction measurements, the pellets were pulverized mechanically and sealed in controlled atmosphere. A hydrated sample was prepared using heavy water D_2O , to minimize the incoherent background from H, and for better contrast of D for NPD. This was done by heating the dry powder up to 300 °C in wet (D_2O) Ar atmosphere ($p\text{D}_2\text{O} = 0.025 \text{ atm}$) and kept there for 20 h. Subsequently, the sample was cooled down to room temperature in dry atmosphere to avoid condensation and formation of surface water. The wet atmosphere was obtained by bubbling Ar at room temperature first through pure D_2O and then through a saturated solution of KBr in D_2O .

X-ray Powder Diffraction. The patterns were collected using $\text{Cu K}_{\alpha 1\&\alpha 2}$ radiation in a Bruker AXS D8 Advance diffractometer equipped with a Gobel mirror and a LynxEyeTM 1D strip detector at room temperature. The samples were packed in boron glass capillaries (0.3 mm Ø) and sealed in a glovebox filled with purified Ar (<1 ppm O_2 , H_2O). Data acquisition collected on rotating capillaries was restricted to the $8^\circ \leq 2\theta \leq 90^\circ$ range with step-size of 0.015°.

Neutron Powder Diffraction. The NPD studies were performed at elevated temperatures (20–700 °C) at E9, the high-resolution powder neutron diffractometer ($\lambda = 1.7973 \text{ \AA}$), located at the BER II research reactor at the Helmholtz-Centre Berlin (former Hahn-Meitner-Institute).¹⁹ For the measurements at 20 and 400 °C, the powder was sealed into a cylindrical vanadium sample container with diameter of 8 mm. For the measurement at 700 °C, the sample was sealed into a quartz tube of 8 mm inner diameter, and an insert of gold foil (0.025 mm thickness) was used to prevent chemical reaction between the quartz and the sample. Because of the high incoherent cross section of hydrogen, very low hydrogen content ($[\text{OH}] < 1 \text{ ppm}$) quartz (SUPRASIL) was used to reduce the background contribution of the sample mounting. The diffraction patterns were analyzed with the Fullprof Rietveld refinement package software.²⁰ The peak shapes were fitted with Thompson–Cox–Hastings pseudo-Voigt convoluted with axial divergence asymmetry function and the backgrounds were fitted with 12-coefficients Fourier cosine series over the whole 2θ range.

DFT Calculations. Periodic calculations based on density functional theory were performed as implemented in the Vienna ab initio software package (VASP).²¹ A plane wave basis set with a cutoff energy of 800 eV and the Perdew–Burke–Ernzerhof (PBE)²² exchange-correlation functional in its spin polarized version were used for relaxations and total energy calculations. The projector-augmented wave (PAW) method within the frozen core approximation was used to describe the electron–core interaction,²³ and we considered Sr electrons up to 3d and Ta up to 5s as the core. The Brillouin zone was mapped by a $9 \times 9 \times 9$ k-points grid within the Monkhorst-Pack scheme.²⁴ Convergence of the electronic structures was ensured by requiring the energy difference in the self-consistent cycle to be below 10^{-6} eV .

Simultaneous relaxation of the lattice constants and atomic position was performed, and the structures were considered as relaxed when the Hellmann–Feynman forces reached a threshold of 0.05 eV/Å. A 0.05 eV wide Gaussian smearing

for the electronic occupation was used for the relaxations, while final electronic structure calculations were performed using the linear tetrahedron method with Blöchl corrections.²⁵

Ab initio molecular dynamics (MD) simulations were performed using DFT, but with the settings described above being reduced in order to keep the computational cost of the simulations affordable. In our tests, an energy cutoff of 300 eV and a single \mathbf{k} point (the Γ point) were enough to give correct forces within ~ 0.1 eV/ \AA compared to the higher accuracy calculations acting on the ions. A canonical ensemble (NVT) approach and spin unpolarized functionals were used for the MD calculations.

RESULTS AND DISCUSSION

Structure for $\text{Sr}_6\text{Ta}_2\text{O}_{11}$. As a starting geometry for DFT calculations, a double perovskite structure was built at its full occupancy. The unit cell, corresponding to two formula units of the hypothetical $\text{Sr}_6\text{Ta}_2\text{O}_{12}$ with a total of 40 atoms, was then subject to a full geometry optimization of the ionic positions and lattice vectors. Figure 1 shows the obtained result: a cubic

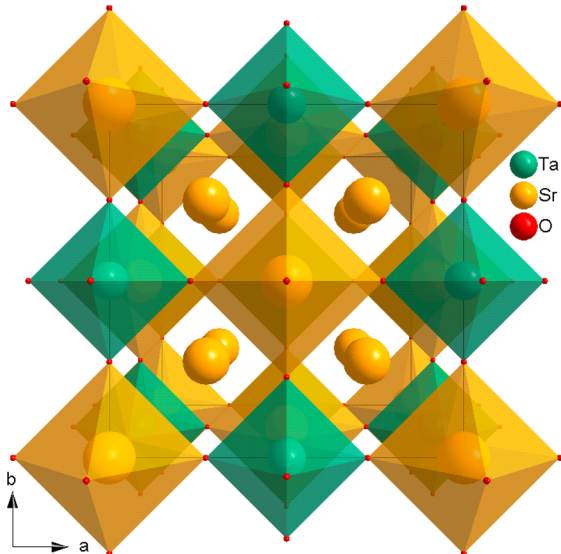


Figure 1. The structure of $\text{Sr}_6\text{Ta}_2\text{O}_{12}$ from DFT calculations.

structure with lattice constant $a = 8.698 \text{ \AA}$ and space group $Fm\bar{3}m$ in which the Ta octahedra are slightly more contracted with respect to the Sr ones, the interatomic distances are $d(\text{Ta}-\text{O}) = 1.99 \text{ \AA}$ and $d(\text{Sr}-\text{O}) = 2.36 \text{ \AA}$. We then built a $\text{Sr}_6\text{Ta}_2\text{O}_{11}$ cell by introducing oxygen vacancies, that is, removing 1 oxygen atom per formula unit from the $\text{Sr}_6\text{Ta}_2\text{O}_{12}$ structure obtained above. All the atomic positions were then relaxed to new equilibrium positions. This resulted in a structure with significantly lower symmetry, namely tetragonal within space group $P4/nmm$ (cell $a = 8.901 \text{ \AA}$, $b = c = 8.545 \text{ \AA}$), though we point out that oxygen vacancies in this model are necessarily ordered due to the periodic boundary conditions used in the calculation. The computed $\text{Sr}_6\text{Ta}_2\text{O}_{11}$ lattice structure is shown in Figure 2. The oxygen and A site Sr atoms are shifted toward the vacancy with respect to the $\text{Sr}_6\text{Ta}_2\text{O}_{12}$ structure.

The XRPD pattern at 20 °C and NPD patterns at 20, 400, and 700 °C of $\text{Sr}_6\text{Ta}_2\text{O}_{11}$ are shown in Figure 3. No major changes can be noted between the NPD patterns; the additional peaks in the 700 °C data are indexed to the gold pattern, arising from the gold insert, and the higher background

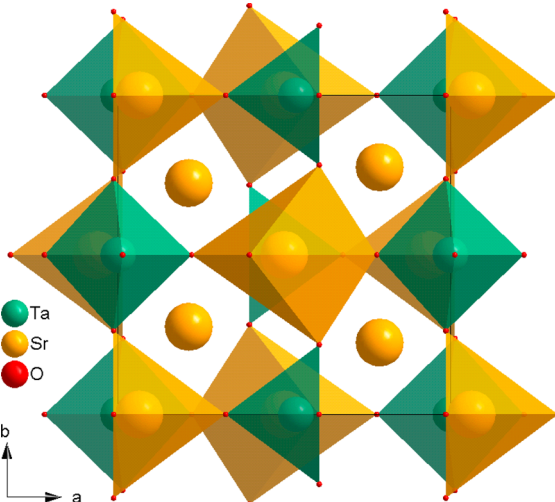


Figure 2. The structure of $\text{Sr}_6\text{Ta}_2\text{O}_{11}$ from DFT calculations.

is due to the quartz sample holder. The peak positions are shifted toward lower angles while heating due to thermal expansion of the compounds. Furthermore, the peak intensities of some reflections are varying as a function of temperature, which may indicate changes in occupancies of atomic sites. In the NPD patterns, the existence of a secondary phase, namely cubic SrO , is observed. The red vertical lines in the Figure 3a indicate the reflections arising from SrO . The secondary phase was not observed in the XRPD pattern, since the common laboratory XRPD used cannot distinguish such a minor phase. High diffuse background of the NPD patterns, but not of the XRPD pattern, is similar to what has been observed for various oxide ion conductors by NPD,^{26–29} and it has been described as substantial disorder of the oxygen sublattice.

The XRPD data was successfully indexed and refined (see Figure 4) with a previously suggested cubic model,¹⁶ $Fm\bar{3}m$, $a = 8.31615(19)$, (RF-factor $\sim 7.96\%$), which was also the model obtained by DFT calculations for the model composition $\text{Sr}_6\text{Ta}_2\text{O}_{12}$. This space group was then used for tentative refinements of the NPD data at 20 °C, however, giving rather bad results with RF-factor of about 18%. The tetragonal space group $P4/nmm$ obtained as a result of the DFT calculations was tested, but the refinements ruled it out as a feasible solution. A previously reported model, hexagonal $\bar{6}2m$, based on the TEM results,¹⁸ was also tested without any better success. A recent report about a related compound $\text{Sr}_{6-2x}\text{Nb}_{2+2x}\text{O}_{11+3x}$ ²⁶ suggests a new structural model with the cubic space group $Fm\bar{3}m$ including additional oxygen sites for such ion conducting cubic perovskites. Additional oxygen sites at Wyckoff position 96j were therefore added into the model (hereafter called O2 sites), improving the refinements remarkably. Also more freedom was given to the oxygen atoms located at the octahedral coordination around the B site cations, using the Wyckoff position 96k instead of 24e; these sites are hereafter called O1 sites. Reasonable refinements were obtained with such a model, giving an R-factor of 8.08%. The refinement is shown in Figure 5, and the results are given in Table 1. The obtained occupancy for the O1 site is 15.6%, for the O2 site 7.12%, and for the A site Sr cation 98%; the molecular formula for the refined composition can then be written as $\text{Sr}_{3.9}(\text{Sr}_2\text{Ta}_2)\text{O}_{10.9}$. An illustration of the structure is presented in Figure 6. The O1 sites are presented as full red circles, and the O2 sites are presented as red outlined circles with crosses. The O1 sites are

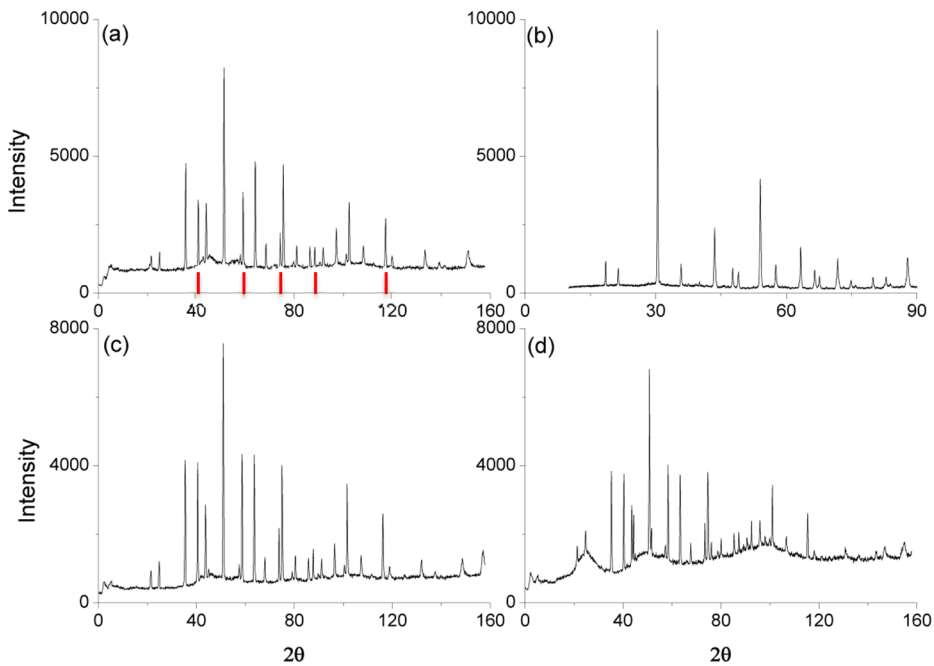


Figure 3. Diffraction patterns of $\text{Sr}_6\text{Ta}_2\text{O}_{11}$ (a) NPD at 20 °C, (b) XRPD at 20 °C, (c) NPD at 400 °C, and (d) NPD at 700 °C. The red vertical lines in (a) point out the reflections rising from the cubic secondary phase SrO .

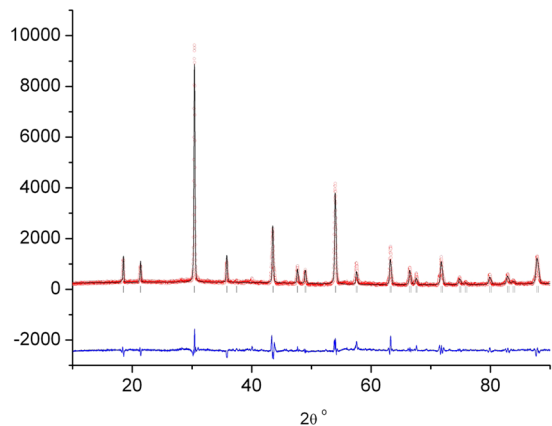


Figure 4. Rietfeld refinement of the XRPD data.

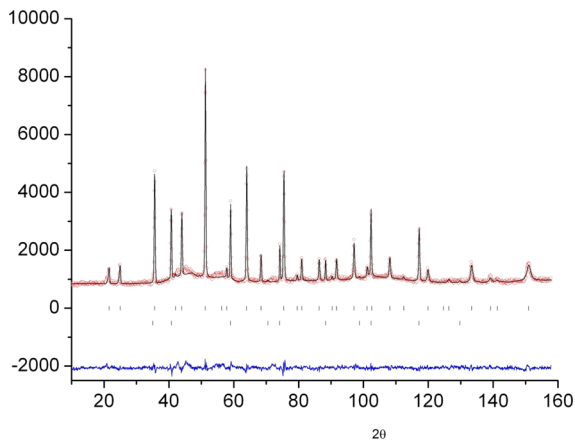


Figure 5. Rietfeld refinement of the NPD data.

in an arrangement similar to octahedral coordination around the B site cations, whereas each corner has four possible

locations. Because of the low occupancy of the O1 sites, less than four out of six octahedral corners are occupied. The location of the vacant O1 sites could not be identified, and therefore we assume that they are statistically distributed, that is, no ordering of the vacancies exists at room temperature. About 30% of the oxygen atoms in this compound are located at O2 sites, around the A site Sr cations. Subsequently, the NPD data at 400 and 700 °C were refined using this structural model; results are given in Tables 2 and 3, respectively. The overall structure remains substantially the same. Besides the normal thermal expansion, we observe increasing deficiency at the O1 and O2 sites and at the cation A site.

The structure of the model composition of the hypothetical $\text{Sr}_6\text{Ta}_2\text{O}_{12}$ obtained from DFT calculations is similar to that one obtained from XRPD and NPD refinements for $\text{Sr}_6\text{Ta}_2\text{O}_{11}$. The main difference is that the NPD refinements suggest additional structural oxygen sites (O2 sites) with fractional occupancy and fractional occupancy of the O1 site with slight variation around the predicted octahedral positions. The occurrence of the O2 sites does not change the space group or the lattice parameters. As these additional oxygen sites have low occupancy, it is obviously a challenge to observe them by standard laboratory XRPD. The reasons why DFT calculations could not indicate such sites can be various. First of all, DFT calculations always present the situation at 0 K. We have chosen to perform our diffraction studies at higher temperatures in order to understand the structural features of this material in context with the ionic conductivity. Also, standard DFT calculations cannot consider partial occupancy of lattice sites and therefore we could not test the stability and occupancy of the O2 sites by DFT methods.

Therefore, we performed ab initio molecular dynamic simulations at 500 and 1000 K in order to extend our DFT results. The total time of the simulation was 9 ps, while the time step was set to 2.25 fs. Nevertheless, the resulting pair distribution functions did not show any counts at a Sr–O distance compatible with O2 sites. The DFT calculations

Table 1. Refinement Results of $\text{Sr}_6\text{Ta}_2\text{O}_{11}$ Obtained from NPD at 20 °C^a

atom	Wyckoff notation	x	y	z	occupancy	B (Å ²)
Sr1	4a	0	0	0	1	11.012(303)
Sr2	8c	0.25	0.25	0.25	0.816	5.609(165)
Ta	4b	0.5	0.5	0.5	1	2.175(95)
O1	96k	0.0261(8)	0.0261(8)	0.2418(13)	0.145	2.902(301)
O2	96j	0.3627(24)	0.5	0.190(2)	0.068	4.813(513)

^aSpace group $Fm\bar{3}m$. Lattice constants $a = b = c = 8.38127(16)$ Å. Composition $\text{Sr}_{5.3}\text{Ta}_2\text{O}_{10.2}$. Crystalline mole percent composition: $\text{Sr}_{5.3}\text{Ta}_2\text{O}_{10.2}/\text{SrO}/\text{Au} = 63.6/25.5/10.9\%$. $\chi^2 = 2.04$; Rf($\text{Sr}_{5.3}\text{Ta}_2\text{O}_{10.2}$) = 8.61%; Rf(SrO) = 7.10%; Rf(Au) = 9.72%.

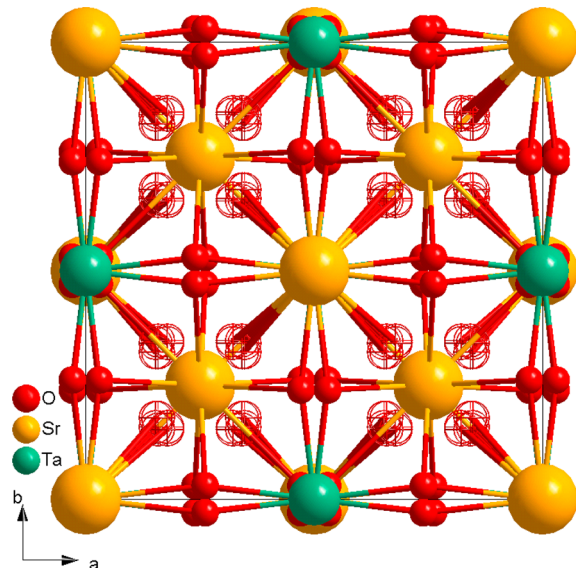


Figure 6. Structure of $\text{Sr}_6\text{Ta}_2\text{O}_{11}$ obtained from NPD. O₁ sites are shown as filled red balls and O₂ site are shown as outlined red circles with crosses.

provided a result with ordered oxygen vacancies for the composition $\text{Sr}_6\text{Ta}_2\text{O}_{11}$. This was also the observation in the TEM studies,¹⁸ which were performed under conditions very different to the NPD measurements.

At low temperatures, the oxygen vacancies order so that the distance between them is the largest possible. At higher temperatures, the structural picture gets more complex; octahedral O1 site positions are getting perturbed and besides additional O2 sites become evident. With increasing temperatures, the occupancies of both these oxygen sites are decreasing. The composition of the material is changing as a function of temperature, following the trend observed by Spitsyn et al.,³⁰ who discussed the complex temperature dependent phase equilibria of $\text{SrO}-\text{Ta}_2\text{O}_5$ and other alkaline earth metal niobate and tantalate systems. The full phase diagram over temperature is not available for our system, but for instance a clear temperature dependency of the phase

equilibria for systems like $\text{SrO}-\text{Nb}_2\text{O}_5$ shows similar features to what we observe as a result of NPD refinements in our study. The Sr depletion takes place on the A cation site, in our refinements called Sr1 sites, with enormous thermal displacement parameters. These results together with the high background observed in the NPD patterns indicate increasing disorder in the oxygen sublattice in combination with perturbations at the Sr1 site. The thermal evolution of the composition and the structural changes can be understood following the explanation of Deniard et al.,²⁷ the oxygen vacancy influences its surroundings so that the atomic displacement of O1 and Sr1 become anharmonic. In our DFT results, a corresponding effect was seen as a shift of the Sr1 and O1 atoms toward the oxygen vacancy. At higher temperatures, the anharmonicity would introduce distortions that will eventually lead to deficiency of atoms at Sr1 and O1 sites and further generate a new structural picture with additional O2 sites of fractional occupancy.

Structure of $\text{Sr}_6\text{Ta}_2\text{O}_{10}(\text{OH})_2$. We performed NPD measurements of the hydrated form using D_2O instead of H_2O for better contrast and lower incoherent background. The secondary phase SrO would also be deuterated into $\text{Sr}(\text{OD})_2$ and refinement of the combined pattern was impossible. The NPD pattern at $T = 20$ °C of $\text{Sr}_6\text{Ta}_2\text{O}_{10}(\text{OD})_2$ is shown in Figure 7 in comparison with the corresponding pattern of the dry $\text{Sr}_6\text{Ta}_2\text{O}_{11}$. Despite the problems to refine the deuterated structure, we can draw some conclusions from the similar diffuse backgrounds observed for both dry and deuterated samples, indicating analogous disorder on the oxygen and strontium sublattices. This is interesting because the distortions of the oxygen and strontium sublattices for the dried sample are resulting from the oxygen vacancy; it is unlikely that protons/deuterons would generate a similar effect. Therefore, the picture of the hydrated sample at higher temperatures would include components such as disorder on oxygen and strontium sublattices, additional O2 sites, vacancies on O1, O2, and Sr1 sites, and protons/deuterons.

A model structure for the hydrated compound $\text{Sr}_6\text{Ta}_2\text{O}_{10}(\text{OH})_2$ was tentatively generated from the structure of $\text{Sr}_6\text{Ta}_2\text{O}_{12}$ described above. In the DFT calculations, four

Table 2. Refinement Results of $\text{Sr}_6\text{Ta}_2\text{O}_{11}$ Obtained from NPD at 400 °C^a

atom	Wyckoff notation	x	y	z	Occupancy	B (Å ²)
Sr1	4a	0	0	0	1	6.405(229)
Sr2	8c	0.25	0.25	0.25	0.95	5.476(118)
Ta	4b	0.5	0.5	0.5	1	1.845(96)
O1	96k	0.0282(4)	0.0282(4)	0.2336(5)	0.15	1.012(188)
O2	96j	0.3654(14)	0.5	0.191(1)	0.07	1.347(385)

^aSpace group $Fm\bar{3}m$. Lattice constants $a = b = c = 8.34585(12)$ Å. Composition $\text{Sr}_{5.8}\text{Ta}_2\text{O}_{10.6}$. Crystalline mole percent composition: $\text{Sr}_{5.8}\text{Ta}_2\text{O}_{10.6}/\text{SrO} = 69.4/30.6\%$. $\chi^2 = 2.71$; Rf($\text{Sr}_{5.8}\text{Ta}_2\text{O}_{10.6}$) = 6.81%; Rf(SrO) = 5.65%.

Table 3. Refinement Results of $\text{Sr}_6\text{Ta}_2\text{O}_{11}$ Obtained from NPD at 700 °C^a

atom	Wyckoff notation	x	y	z	occupancy	B (Å ²)
Sr1	4a	0	0	0	1	7.017(328)
Sr2	8c	0.25	0.25	0.25	0.976	4.855(115)
Ta	4b	0.5	0.5	0.5	1	1.141(89)
O1	96k	0.0279(4)	0.0279(4)	0.2337(6)	0.156	0.321(189)
O2	96j	0.362(1)	0.5	0.189(1)	0.0712	0.578(389)

^aSpace group $Fm\bar{3}m$. Lattice constants $a = b = c = 8.30026(13)$ Å. Composition $\text{Sr}_{5.9}\text{Ta}_2\text{O}_{11.05}$. Crystalline mole percent composition: $\text{Sr}_{5.9}\text{Ta}_2\text{O}_{11.05}/\text{SrO} = 77.9/22.1\%$. $\chi^2 = 2.68$; Rf($\text{Sr}_{5.92}\text{Ta}_2\text{O}_{10.9}$) = 8.08%; Rf(SrO) = 6.33%.

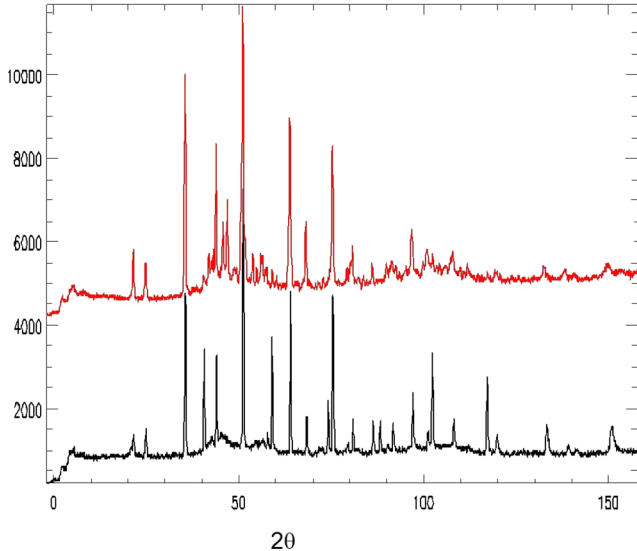


Figure 7. NPD patterns of $\text{Sr}_6\text{Ta}_2\text{O}_{10}(\text{OD})_2$ (above) and $\text{Sr}_6\text{Ta}_2\text{O}_{11}$ (below).

hydrogen atoms have been added to a supercell containing two formula units in order to respect the given stoichiometry. Several combinations of hydrogen placed at Wyckoff 96j positions were tested, following the trends of previously reported H/D positions in similar compounds.^{31–33} After relaxation of both ionic positions and lattice vectors, only minimal deviations from the cubic symmetry were found. The most stable structure obtained from the calculations was within space group Cm , shown in Figure 8. The energy gain in the transition from cubic to monoclinic is 0.44 eV per formula unit. The deviation from 90° angles is less than 2°, which is smaller than the numerical uncertainty of the relaxation procedure; there is thus a possibility that the structure actually is orthorhombic. Lattice positions obtained from DFT optimization are shown in Table 4. From Figure 8, it is possible to see how all the octahedra are tilted and distorted with the both B site cations shifted away from the hydrogen atom. Contrary the A site Sr atom positions shift toward hydrogen. The hydrogen atom forms a 0.99 Å long covalent bond with one oxygen atom in the (100) direction along the edge of a Ta octahedron.

CONCLUSIONS

The archetype $\text{Sr}_6\text{Ta}_2\text{O}_{11}$ has a tetragonal symmetry with ordered oxygen vacancies at low temperatures. The oxygen vacancy introduces anharmonicity to the thermal displacement parameters evolving to increasing distortions on the oxygen and strontium sublattices. At room temperature and above, additional structural oxygen sites are found with fractional occupancy. The high-temperature phases have higher symmetry (cubic) because the oxygen vacancies are statistically

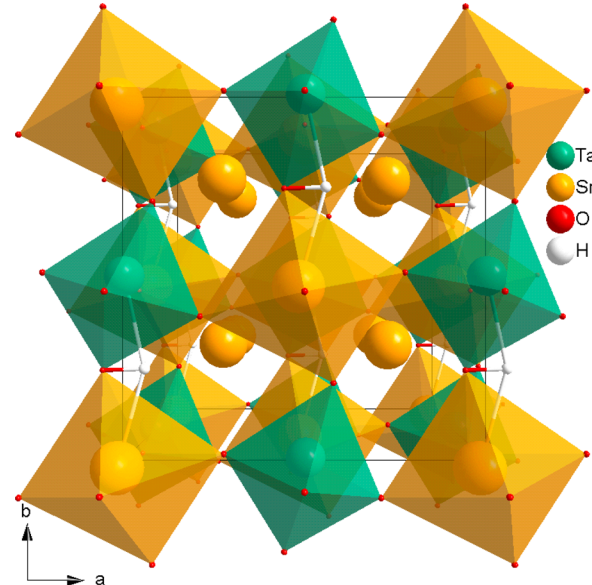


Figure 8. Structure of $\text{Sr}_6\text{Ta}_2\text{O}_{10}(\text{OH})_2$ obtained from DFT calculations.

Table 4. Crystallographic Data of $\text{Sr}_6\text{Ta}_2\text{O}_{11}(\text{OH})_2$ Obtained from DFT Calculations^a

atom	Wyckoff notation	x	y	z
Sr ₁	4b	0.25033	0.31116	0.22190
Sr ₂	4b	0.75033	0.81116	0.22810
Sr ₃	2a	0.98702	0.99082	0
Sr ₄	2a	0.48702	0.4908	0
Ta ₁	2a	0.51025	0.00849	0
Ta ₂	2b	0.0102	0.5085	0
O ₍₁₎	2a	0.21400	0.39807	0
O ₍₂₎	2a	0.71400	0.89807	0
O ₍₃₎	2a	0.07227	0.70458	0
O ₍₄₎	2a	0.57227	0.20458	0
O ₍₅₎	2a	0.27935	-0.00004	0
O ₍₆₎	2a	0.77935	0.49996	0
O ₍₇₎	2a	0.44038	0.73991	0
O ₍₈₎	2a	0.94038	0.23991	0
O ₍₉₎	4b	0.50530	0.96085	0.22325
O ₍₁₀₎	4b	0.00530	0.46085	0.22325
H ₍₁₎	2a	0.05547	0.26418	0.00000
H ₍₂₎	2a	0.55547	0.76418	0.00000

^aSpace group: Cm . Lattice constants $a = 8.4670$ Å $b = 9.4006$ Å $c = 8.6757$ Å, $\alpha = \beta = 90^\circ$, $\gamma = 91.8586$.

distributed. The disorder of the oxygen sublattice increases with increasing temperatures along with increasing ionic conductivities. The archetype structure of the hydrated compound $\text{Sr}_6\text{Ta}_2\text{O}_{10}(\text{OH})_2$ was obtained by DFT. Protons

can be located at specific sites in the structure, and they distort the structure more than the oxygen vacancies. At higher temperatures, the hydrated material exhibits disordered features and the proton locations could not be addressed.

AUTHOR INFORMATION

Corresponding Author

(N.J.) Tel: +1-865-241-3107. E-mail: n.jalarvo@fz-juelich.de.
(T.N.) Tel: +47-22840654. E-mail: t.e.norby@kjemi.uio.no.

Author Contributions

The manuscript was written through contributions of all authors. All authors have given approval to the final version of the manuscript.

Notes

The authors declare no competing financial interest.

ACKNOWLEDGMENTS

The authors would like to thank Dr. Simon Kimber and Dr. Dimitri N. Argyriou for help with the NPD measurements at E9 and for the discussion about the data interpretation. This work was supported by the FRINAT project 171157/V30 "Hydrogen in oxides (HYDROX)" of the Research Council of Norway and by the European Commission under the seventh Framework Programme through the "Research Infrastructure" action of the "Capacities" Programme, NMI3-II Grant 283883.

REFERENCES

- Goodenough, J. B. Oxide-ion electrolytes. *Annu. Rev. Mater. Res.* **2003**, *33*, 91–128.
- Iwahara, H. Proton conducting ceramics and their applications. *Solid State Ionics* **1996**, *86–88*, 9–15.
- Perovskite Oxide for Solid Oxide Fuel Cells*; Ishihara, T. Ed.; Springer: New York, 2009.
- Norby, T. Solid-state protonic conductors: principles, properties, progress and prospects. *Solid State Ionics* **1999**, *125*, 1–11.
- Iwahara, H.; Esaka, T.; Uchida, H.; Maeda, N. Proton conduction in sintered oxides and its application to steam electrolysis for hydrogen production. *Solid State Ionics* **1981**, *3–4*, 359–363.
- Iwahara, H.; Uchida, H.; Ono, K.; Ozaki, K. Proton Conduction in Sintered Oxides Based on BaCeO₃. *J. Electrochem Soc.* **1988**, *135*, 529–533.
- Kreuer, K. D. Proton conducting Oxides. *Annu. Rev. Mater. Res.* **2003**, *33*, 333–359.
- Animitsa, I.; Norby, T.; Marion, S.; Glöckner, R.; Neiman, A. Incorporation of water in strontium tantalates with perovskite-related structure. *Solid State Ionics* **2001**, *145*, 357–364.
- Schober, T. Phase diagrams in the proton conductor systems Sr₆Ta₂O₁₁nH₂O. *Solid State Ionics* **2006**, *177*, 471–474.
- Animitsa, I.; Neiman, A.; Sharafutdinov, A.; Nochrin, S. Strontium tantalates with perovskite-related structure. *Solid State Ionics* **2000**, *136–137*, 265–271.
- Paulus, W.; Schober, H.; Eibl, S.; Johnson, M.; Bethier, T.; Hernandez, O.; Ceretti, M.; Plazanet, M.; Conder, K.; Lamberti, C. Mobility in Solid Oxide Ion Conductors. *J. Am. Chem. Soc.* **2008**, *130*, 16080–16085.
- Piovano, A.; Agostini, G.; Frenkel, A. I.; Bertier, T.; Prestipino, C.; Ceretti, M.; Paulus, W.; Lamberti, C. Time Resolved in Situ XAFS Study of the Electrochemical Oxygen Intercalation in SrFeO_{2.5} Brownmillerite Structure: Comparison with the Homologous SrCoO_{2.5} System. *J. Phys. Chem. C* **2011**, *115*, 1311–1322.
- Nemudry, A.; Weiss, M.; Gainutdinov, I.; Boldyrev, V.; Schöllhorn, R. Room Temperature Electrochemical Redox Reactions of the Defect Perovskite SrFeO_{2.5+x}. *Chem. Mater.* **1998**, *10*, 2403–2411.
- Karvonen, L.; Valkeapää, M.; Liu, R.-S.; Chen, J.-M.; Yamauchi, H.; Karppinen, M. O-K and Co-L XANES Study on Oxygen Intercalation in Perovskite SrCoO_{3.δ}. *Chem. Mater.* **2010**, *22*, 70–76.
- Le Toquin, R.; Paulus, W.; Cousson, A.; Prestipino, C.; Lamberti, C. Time-Resolved in Situ Studies of Oxygen Intercalation into Absorption Spectroscopy. *J. Am. Chem. Soc.* **2006**, *128*, 13161–13174.
- Animitsa, I.; Nieman, A.; Titova, S.; Kochetova, N.; Isaeva, E. Phase relations during water incorporation in the oxygen and proton conductor Sr₆Ta₂O₁₁. *Solid State Ionics* **2003**, *156*, 95–102.
- Colomban, P.; Romain, F.; Neiman, A.; Animitsa, I. *Solid State Ionics* **2001**, *145*, 339–347.
- Ashok, A. M. Ph.D. thesis, Faculty of Mathematics and Natural Sciences, University of Oslo, Oslo, Norway, 2008.
- Többens, D.; Stüsser, N.; Knorr, K.; Mayer, H. M.; Lampert, G. E9: The New High-Resolution Neutron Powder Diffractometer as the Berlin Neutron Scattering Center. *Mater. Sci. Forum* **2001**, *378–381*, 288–293.
- Rodríguez-Carvajal, J. Recent Advances in Magnetic Structure Determination by Neutron Powder Diffraction. *Physica B* **1993**, *192*, 55–69.
- Kresse, G.; Furthmüller, J. Efficiency of ab-initio total energy calculations for metals and semiconductors using a plane-wave basis set. *Comput. Mater. Sci.* **1996**, *6*, 15–50.
- Perdew, J. P.; Burke, K.; Ernzerhof, M. Generalized gradient approximation made simple. *Phys. Rev. Lett.* **1996**, *77*, 3865–3868.
- Kresse, G.; Joubert, D. From ultrasoft pseudopotentials to the projector augmented-wave method. *Phys. Rev. B* **1999**, *59*, 1758–1775.
- Monkhorst, H. J.; Pack, J. D. On Special Points for Brillouin Zone Integrations. *Phys. Rev. B* **1976**, *13*, 5188–5192.
- Blöchl, P. E.; Jepsen, O.; Andersen, O. K. Improved tetrahedron method for Brillouin-zone integrations. *Phys. Rev. B* **1994**, *49*, 16223–16233.
- Li, M.-R.; Hong, S.-T. Interstitial Oxygen in Perovskite-Related Sr_{6-2x}Nb_{2+2x}O_{11+3x}. *Chem. Mater.* **2008**, *20*, 2736–2741.
- Deniard, P.; Caldes, M. T.; Zou, X. D.; Diot, N.; Marchand, R.; Brec, R. Structural Modulation in Sr_{1.4}Ta_{0.6}O_{2.9}: non-harmonicity on ADPs during Rietveld refinement. *Int. J. Inorg. Mater.* **2001**, *3*, 1121–1123.
- Goutenoire, F.; Isnard, O.; Suard, E.; Bohnke, O.; Laligant, Y.; Retoux, R.; Lacorre, P. Structural and transport characteristics of the LAMOX family of fast oxide-ion conductors, based on lanthanum molybdenum oxide La₂Mo₂O₉. *J. Mater. Chem.* **2001**, *11*, 119–124.
- Aguadero, A.; Martínez-Lope, M. J.; Pomjakushin, V.; Alonso, J. A. Oxygen-Deficient R₂MoO_{6-δ} (R = Tb, Dy, Y, Ho, Er, Tm, Yb) with Fluorite Structure as Potential Anodes in Solid Oxide Fuel Cells. *Eur. J. Inorg. Chem.* **2011**, *21*, 3226–3231.
- Spitsyn, V. I.; Ippolitova, E. A.; Kovba, L. M.; Lykova, L. N.; Lshenko, P. P. *Russ. J. Inorg. Chem.* **1982**, *27*, 827–832.
- Sosnowska, I.; Przenioslo, R.; Schäfer, W.; Kockelmann, W.; Hempelmann, R.; Wysocki, K. Possible deuterium positions in the high-temperature deuterated proton conductor Ba₃C_{1+y}Nb_{2-y}O_{3-d} studied by neutron and X-ray powder diffraction. *J. Alloys Compd.* **2001**, *328*, 226–230.
- Shimoyama, T.; Tojo, T.; Kawaji, H.; Atake, T.; Igawa, N.; Ishii, Y. Determination of deuterium location in Ba₃Ca_{1.18}Nb_{1.82}O_{8.73}. *Solid State Ionics* **2008**, *179*, 231–235.
- Ahmed, I.; Knee, C. S.; Karlsson, M.; Eriksson, S. G.; Henry, P. F.; Matic, A.; Engberg, D.; Börjesson, L. Location of deuteron sites in the proton conducting perovskite BaZr_{0.50}In_{0.50}O_{3-y}. *J. Alloys Compd.* **2008**, *450*, 103–110.